Bioinspired kirigami metasurfaces as assistive shoe grips

Sahab Babaee[1,2,7], Simo Pajovic[1,2,3,7], Ahmad Rafsanjani [4,7], Yichao Shi[2,3], Katia Bertoldi [5 ✉] and Giovanni Traverso [1,2,6 ✉]

---

[1]Department of Mechanical Engineering, Massachusetts Institute of Technology, Cambridge, MA, USA. [2]Department of Chemical Engineering and Koch Institute for Integrative Cancer Research, Massachusetts Institute of Technology, Cambridge, MA, USA. [3]Department of Mechanical and Industrial Engineering, University of Toronto, Toronto, Ontario, Canada. [4]Department of Materials, ETH Zurich, Zurich, Switzerland. [5]John A. Paulson School of Engineering and Applied Sciences, Harvard University, Cambridge, MA, USA. [6]Division of Gastroenterology, Department of Medicine, Brigham and Women's Hospital, Harvard Medical School, Boston, MA, USA. [7]These authors contributed equally: Sahab Babaee, Simo Pajovic, Ahmad Rafsanjani. ✉e-mail: bertoldi@seas.harvard.edu; cgt20@mit.edu

Table of Contents

Supplementary Notes

Supplementary Notes

<u>Evaluation of utilized coefficient of friction on an inclined surface</u>

We have conducted further experiments to evaluate utilized coefficient of friction using an inclined surface. The ice surface was mounted on top of the 51×51 cm force plate with an ascending inclined angle, $\theta = 5°$ (Fig. S7). F_x and F_z are the ground reaction forces in x- and z-directions recorded by the force plate during walking over the half of a gait cycle. The utilized coefficient of friction (μ) was then calculated by:

$$\mu = \frac{F_t}{F_n} = \frac{F_x cos\theta + F_z sin\theta}{F_z cos\theta - F_x sin\theta}$$

, where F_t and F_n are the reaction forces in t- and n-directions. The detailed protocol of gait trials and instruction to the subject for walking on the inclined surface were the same as flat surfaces, described in the Methods section.

<u>Kirigami shoe grips with biaxial friction control</u>

Fig. S8A shows the design of two triangle kirigami structures with symmetric and asymmetric arrays of spikes. In the asymmetric design, the rows of tips of each spike are alternately shifted by the quarter of the unit cell's width to the right and left. We prototyped the kirigami out of 0.127 mm thick polyester plastic shim stock (Artus Corporation, NJ), and performed friction tests using the custom-built friction set-up (see fig. S4 and "Friction testing" in Methods). The kirigami were stretched $\varepsilon_{22} = 0.15$ in 2-direction (Fig. S8B) that results in buckling out of the spikes, and then clamped to the sled with 5 kg weight on the top. The sled was pulled at a constant velocity of 10 mm/s in the 2-direction until reaching the end of the hardwood surface. Then, to evaluate the friction forces in the lateral direction, we repeated the same test by pulling the sled in the 1-direction. In Fig. S8C, we reported the friction forces (F_f) between kirigami (prestretched at $\varepsilon_{22} = 0.15$) with symmetric (left plot) and asymmetric (right plot) arrays of spikes and a hardwood surface as a function of displacement. F_f^1 and F_f^2 are the recorded friction forces in the 1- and 2-directions, shown by dashed and solid lines, respectively. Each test was performed three times with the new kirigami, shown by different colors in Fig. S8C. Interestingly, the data demonstrates that not only both kirigami are capable of biaxial friction enhancement, but also the friction forces in the lateral direction (F_f^1) are higher than the forces in the axial direction (F_f^2). This lateral friction enhancement is even more pronounced for the asymmetric kirigami design.

<u>Experimental fatigue testing of the kirigami shoe grips</u>

We carried out fatigue testing to predict the life of steel shoe grips under cyclic tensile loads. An Instron 5942 series Universal Testing System with a 500 N load cell was used to apply cyclic uniaxial loading under strain-controlled conditions to the specimens (kirigami structures). A 2.5 mm thick ice block (300 ×120 mm) was mounted with the dry surface in a vertical orientation in contact with the kirigami surfaces such that the tips of the kirigami spikes

scratched the ice block while the top crosshead of the testing machine pulled or pushed the kirigami. All tests were conducted using a trapezoidal waveform with $\varepsilon_{Applied}^{max} = 0.15$, shown in Fig. S9. To determine the fatigue life, the specimen failure was defined at the point when a 50% drop in the maximum load (compared to the first cycle) or rupture is recorded. In Fig. S9, we reported the peak force in each cycle, F_{max}, versus the number of loading cycles, n, for the kirigami structures with concave, triangle, and convex spike shapes. We found that the concave kirigami prototypes fail at $n{\sim}1700$ cycles, while the triangle and convex kirigami fail at $n{\sim}1100$ and $n{\sim}900$ cycles, respectively.

Effect of material behavior on the response of kirigami shoe grips

We examined the effect of plasticity and investigated the response of both elastic and elastoplastic kirigami structures under uniaxial tensile loads. We performed FE simulations by assuming an elastic-perfectly plastic material model (with yield stress $\sigma_y = 759$ MPa for 301 stainless steel) under cyclic loading (5 cycles), and compared the results to those obtained for purely elastic kirigami sheets. The results reported in Fig. S10 are for steel kirigami patches with concave, triangle, and convex spike shapes characterized by $\gamma = 30^{\circ}$, $\delta/l = 0.15$. Our finding suggests that while the effective stress-strain response of kirigami patches is affected by plasticity beyond out-of-plane buckling regime (Fig. S10A), the plastic strains localized in the hinges are moderate and the residual macroscopic strain is below 2% for all three patterns (Fig. S10B). From a practical point of view, this residual deformation can be beneficial since it potentially increases the friction of unactuated patches. Moreover, the effect of plasticity on tilting angle of kirigami sheets is negligible (Fig. S10C). Although the residual deformations caused by plasticity at the hinges are inevitable, the plastic deformation does not affect the morphology of the emerging 3D pop-ups, as their characteristics e.g. relation between tilting angle and applied strain are found to be unaltered.

Stress-strain response of finite size kirigami under uniaxial tension

We performed finite size simulations for kirigami structures with triangular cut pattern comprised of 16×2, 16×4, 16×6, 16×8 units and compared the results with those obtained from periodic boundary conditions (PBC). For kirigami structures, three deformation regimes are identified: (i) initial linear regime, (ii) out of plane buckling and departure from linearity, and (iii) hardening due to stretching of the hinges. As shown in Fig. S11, the linear regime is similar for all the samples due to in-plane deformation. By increasing the number of unit cells, the critical strain at which the out-of-plane buckling initiates becomes closer to the response of PBC. On the other hand, increasing the number of horizontal unit cells results in constraining more units at the boundaries, which affects the hardening regime. Therefore, through the application of periodic boundary conditions, we avoid the dependency of the presented results on the choice of the number of units and save computational costs. We confirm that for real applications, the periodic boundary condition can be used as a guide while the results of finite size models should also be considered in the final prototypes.
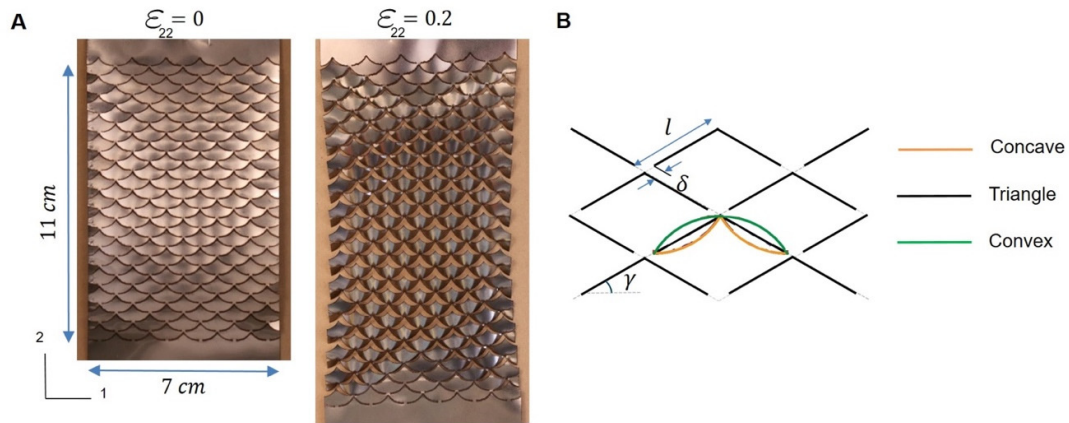
Supplementary Figures

Figure S1: Fabricated steel kirigami shoe grips. (**A**) Undeformed (ε_{22}= 0) and stretched (ε_{22}= 0.2) configurations of the stainless steel kirigami patch made of a periodic array of concave-shaped spikes perforated in one direction. (**B**) The schematics of different spike shapes (in the middle) including concave (orange), triangle (black), and convex (green) with identical cut-angle ($\gamma = 30^o$) and hinge over cut-length ratio ($\delta/l = 0.15$).
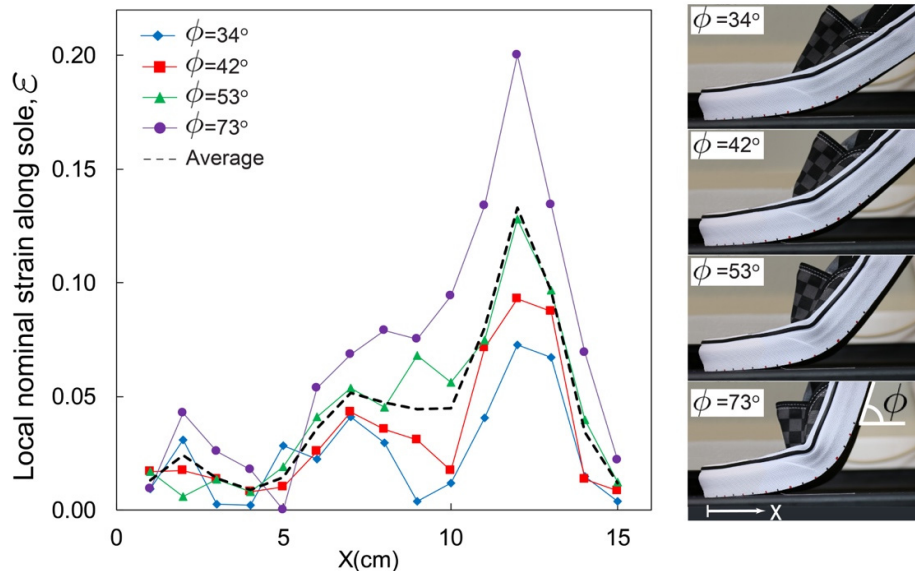

Figure S2: Distribution of strains along a shoe sole over a half gait cycle. The local strains, ε, were reported for different angles between the shoe sole and the walking surface ($\varphi = 34^o$ (blue), 42° (red), 53^o(green), and 73° (purple)) as a function of distance (x) from the shop tip. The snapshots showing the shape of the shoe at the different angles are illustrated on the right.
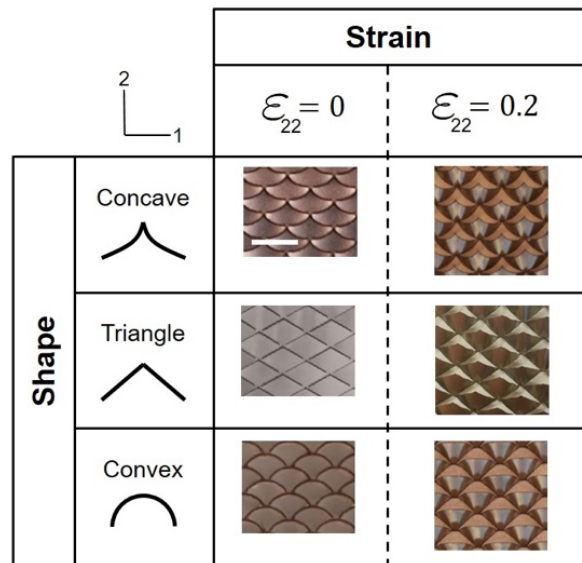
Figure S3: Fabricated kirigami shoe grips with different spike shapes. Undeformed ($\varepsilon_{22}=$ 0) and stretched ($\varepsilon_{22}=0.2$) configurations of the stainless steel kirigami patches with different spike shapes including concave, triangle, and convex that were considered for this study. Scale bar is 10 mm.
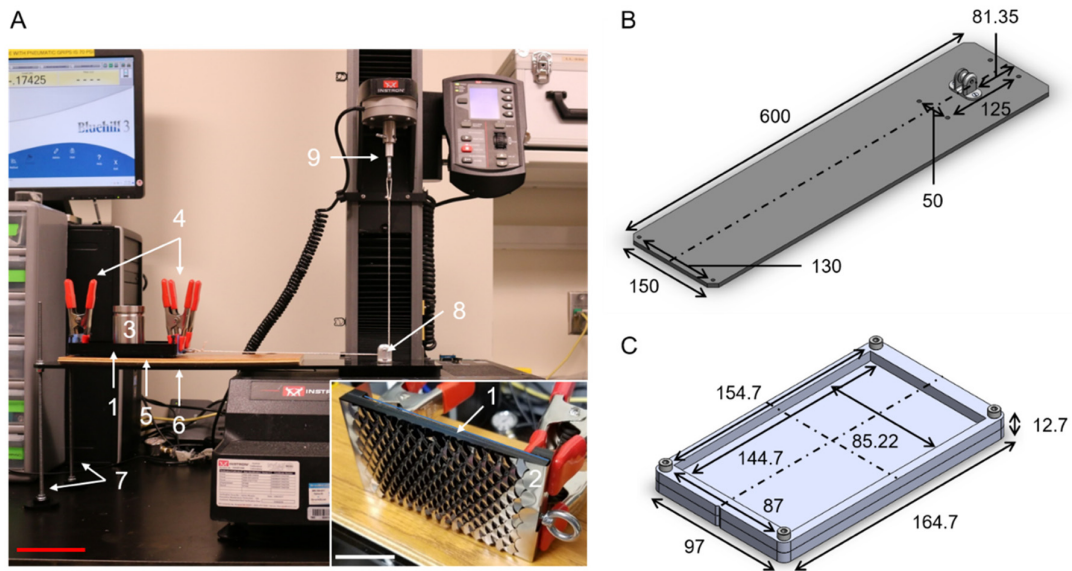
Figure S4: Friction testing set-up. (**A**) A universal testing machine (Instron 5942 series) with a 500 N load cell was used to evaluate the friction properties of the kirigami patches for various surfaces. The set-up (side view in the image) includes: (1) friction testing sled (bottom side shown in inset image) (2) kirigami patch, (3) weight, (4) clamps used to secure kirigami patch in the deformed state at 0.2 strain, (5) test surface (e.g., wood), (6) friction testing table, (7) M6 threaded rods used to support friction testing table, (8) low-friction pulley, and (9) hook attachment for crosshead to pull sled. Red scale bar is 100 mm; white scale bar in inset is 20 mm. The inset image is a bottom view of the friction testing sled with the kirigami patch attached. (1) and (2) are consistent with the outer image. The CAD model of the friction testing table (6) and sled without a kirigami patch (1) are illustrated in an isometric view in (**B**) and (**C**), respectively. All dimensions are in mm.
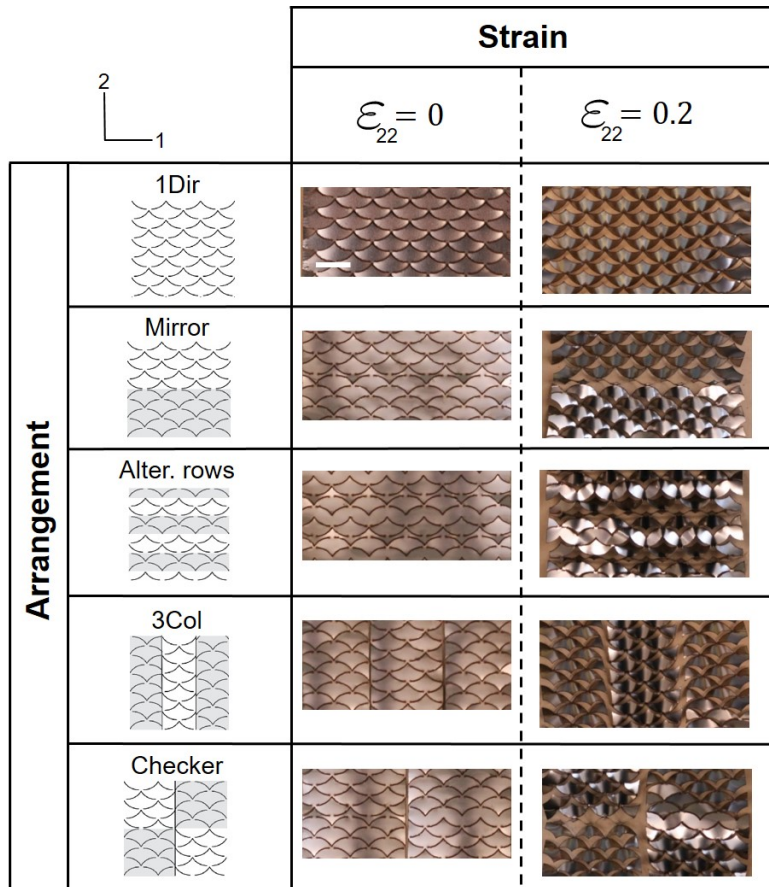
Figure S5: Fabricated steel kirigami shoe grips with different spike arrangements. Undeformed (ε_{22}= 0) and stretched (ε_{22}= 0.2) configurations of the stainless steel kirigami patches with different arrangements of spikes including Unidirectional (1Dir), Mirror, Alternating rows, 3-column, and Checker that were considered for this study. Scale bar is 10 mm.
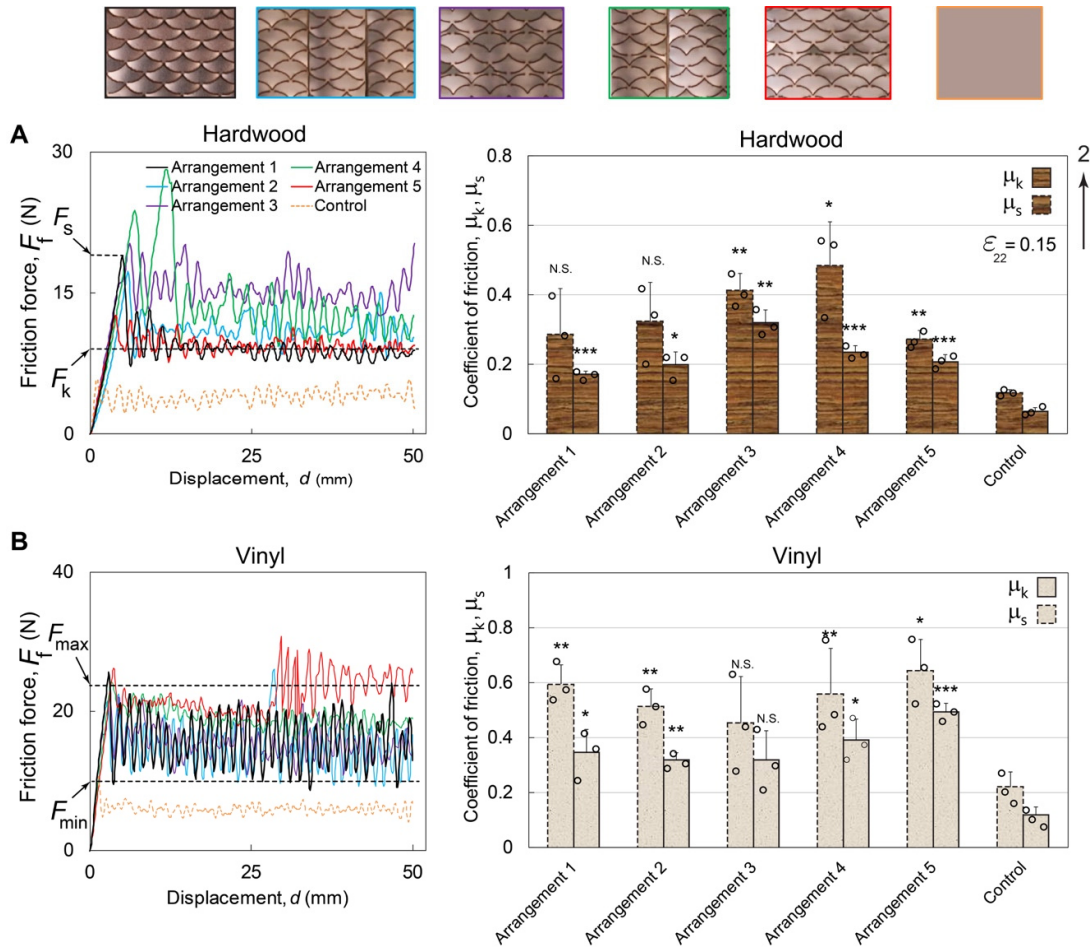
Fig S6. Friction enhancement of the concave kirigami shoe grips with various spike arrangements. Friction force (F_f) vs. displacement (d) response of the concave kirigami surfaces with different spike arrangements prestretched at $\varepsilon_{22} = 0.15$ and control flat surfaces (orange), sliding on (**A**) hardwood, and (**B**) vinyl surfaces. F_s and F_k are the static and kinetic friction forces. Effect of different spike arrangements on static and dynamic friction coefficients (μ_S and μ_K) for kirigami surfaces prestretched at $\varepsilon_{22} = 0.15$ are reported on the right. The different arrangements of the fabricated kirigami grips including arrangement 1 (Unidirectional in black), arrangement 2 (3-column in blue), arrangement 3 (Alternating rows in purple), arrangement 4 (Checker in green), and arrangement 5 (Mirror in red) are shown in the top. Interestingly, all the kirigami demonstrated enhanced frictional properties as compared to the control spikeless patch (orange dashed line), showing the smooth sliding for hardwood and stick-slip response for vinyl. The bar plots show considerable increases in μ_s (two- to three-fold) and μ_k (three- to four-fold) in average for all the arrangements with respect to the controls for both hardwood and vinyl. Data reported as mean ± standard deviation for $n = 3$ measurements for each group. Two-sample t tests were used to determine the significance. *$P < 0.05$, **$P < 0.01$, ***$P < 0.001$, and N.S. not significant (kirigami patch versus control flat surface for both μ_S and μ_K).
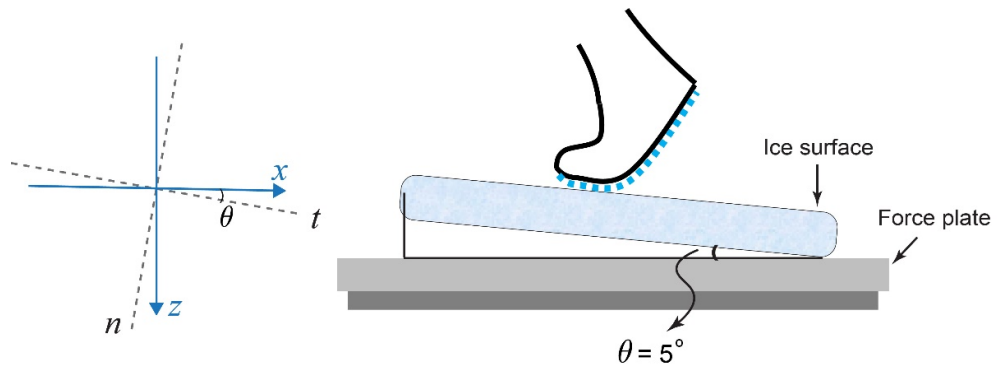
Fig S7. Illustration of force plate testing set-up on an inclined ice surface.
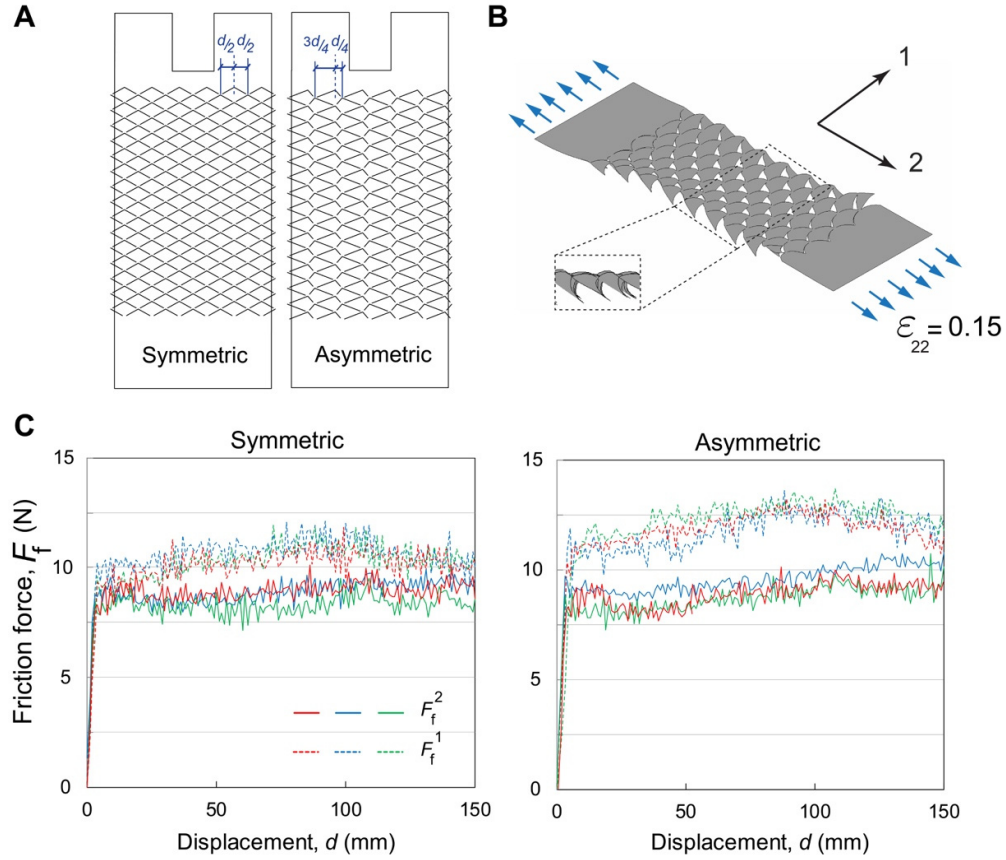
Fig. S8: Biaxial friction control using kirigami surfaces. (**A**) CAD models of triangle kirigami surfaces with symmetric and asymmetric arrays of spikes. d is the width of a unit cell. (**B**) The kirigami can be stretched $\varepsilon_{22} = 0.15$ in 2-direction that results in out of plane buckling of the spikes. (**C**) Friction forces (F_f) between kirigami (prestretched at $\varepsilon_{22} = 0.15$) with symmetric (left plot) and asymmetric (right plot) array of spikes and hardwood surface as a function of displacement. F_f^1 and F_f^2 are the recorded friction forces in 1- and 2-directions, shown by dashed and solid lines, respectively. Each test was performed three times shown by different colors.
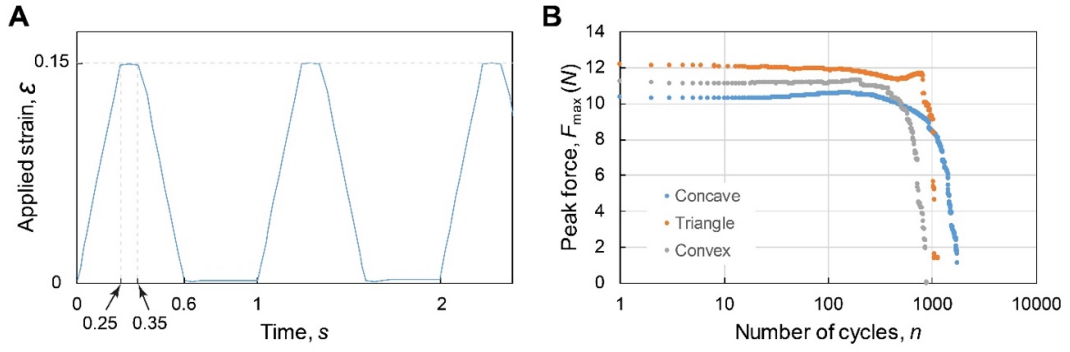
Fig. S9: Experimental fatigue tests. (**A**) Trapezoidal waveform used in the cyclic tests to control the applied strain. (**B**) Maximum recorded applied force, F_{max}, versus the number of loading cycles, n, for the kirigami structures with concave, triangle, and convex spike shapes.
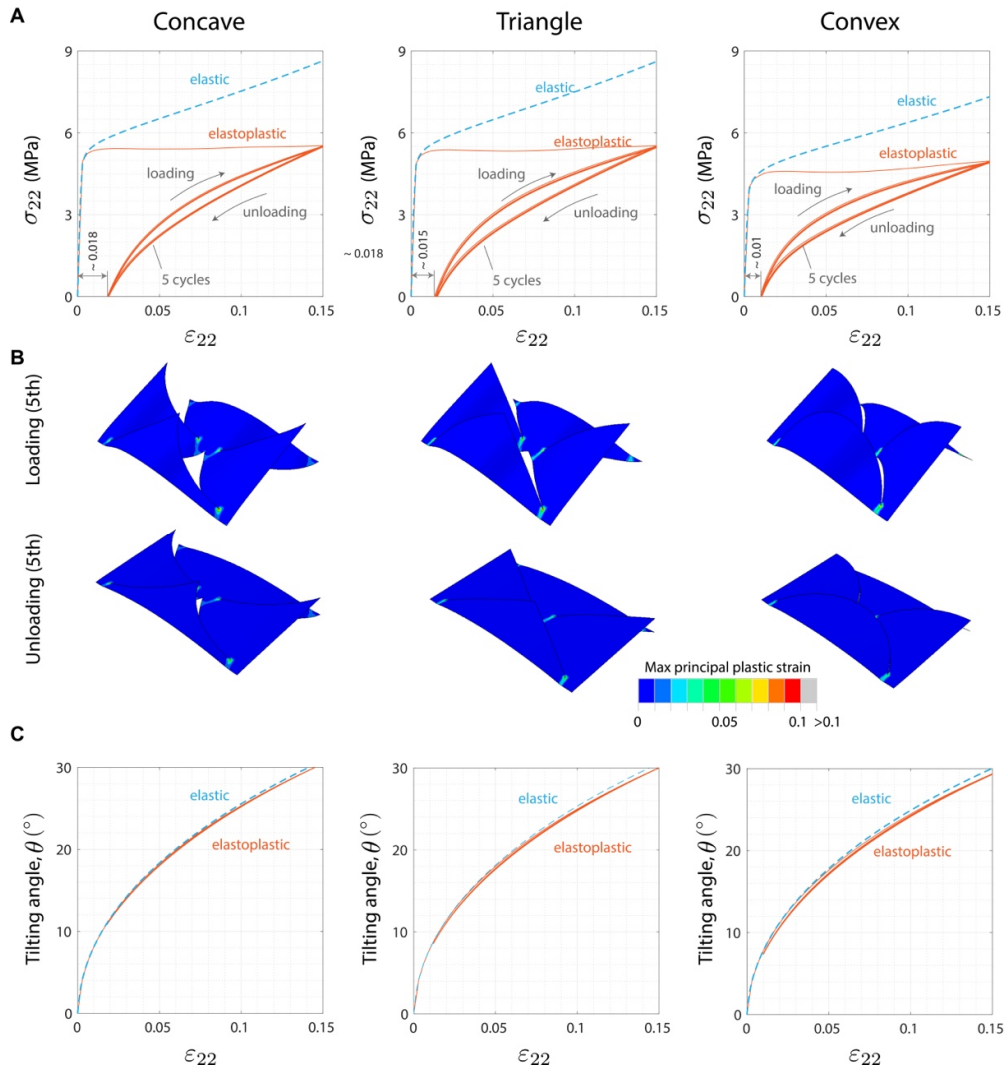
Fig. S10: Effect of material behavior on the response of kirigami structures subjected to uniaxial tension. (**A**) Comparison between numerical stress–strain curves obtained considering a purely elastic (blue dashed lines) and an elastoplastic (orange solid lines for five cyclic loads) material model. Results are reported for concave, triangle, and convex spike shapes steel kirigami patches, characterized by $\gamma = 30^o$, $\delta/l = 0.15$ with the residual macroscopic plastic strains 0.018, 0.015, and 0.010, respectively. (**B**) Snapshots showing the distribution of max principal plastic strains at buckled (loading at $\varepsilon_{22} = 0.15$) and released (unloading at $\varepsilon_{22} = 0$) configurations for 5 cyclic uniaxial tensile loads. (**C**) Comparison between the evolution of tilting angle of the spikes (θ) as a function of applied strain (ε_{22}) for a purely elastic (blue dashed lines) and an elastoplastic (orange solid lines for five cyclic loads) material model.
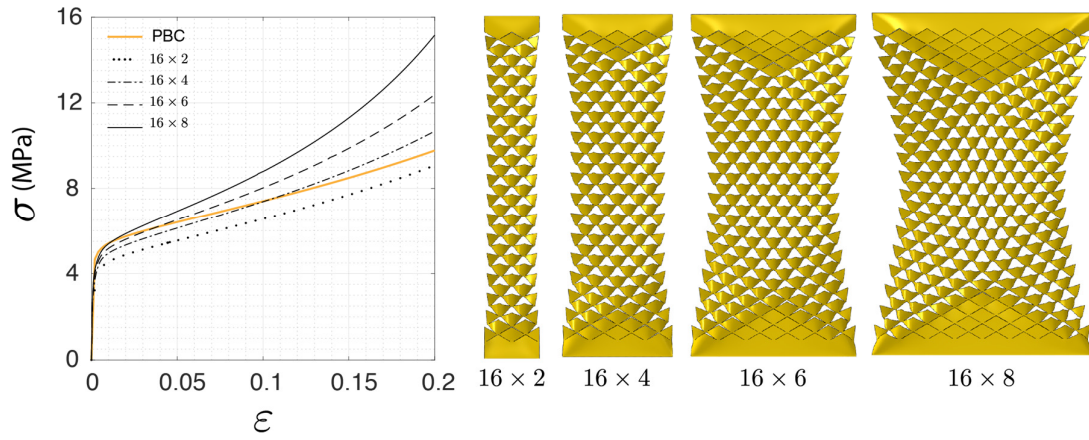
Fig. S11: Stress-strain response of the finite size kirigami under uniaxial tension. Comparison between the response of finite size samples (comprised of 16×2, 16×4, 16×6, 16×8 units) and infinitely large periodic structure (PBC) under uniaxial tension for triangular cut pattern obtained from FEA.
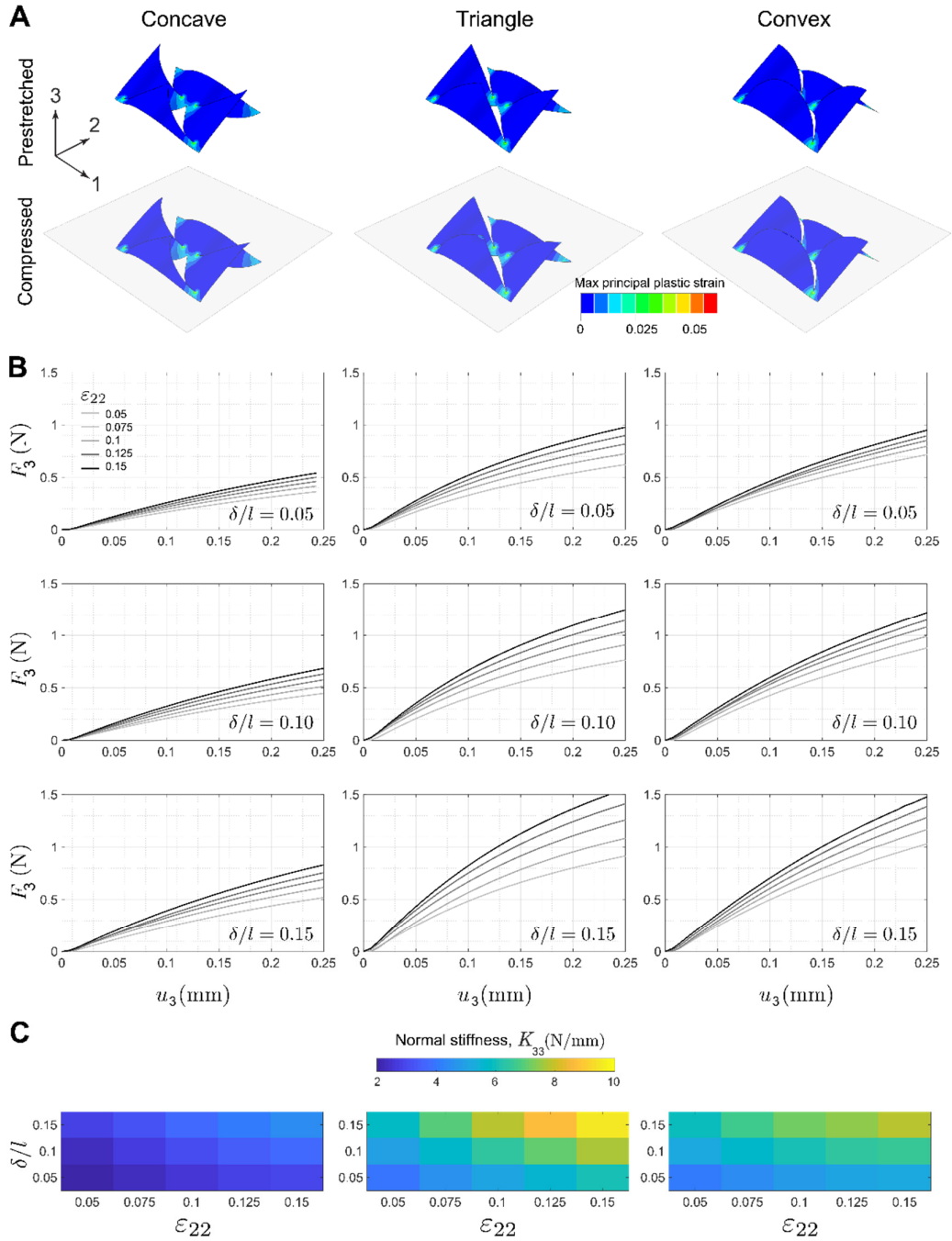
Fig. S12: Evolution of normal stiffness of the kirigami surfaces. (**A**) FEA simulation of periodic kirigami unit cells which are prestretched ($\varepsilon_{22} = 0.15$) and subsequently compressed with a rigid plate. (**B**) Normal force-displacement curves for the different cut patterns and hinge width δ/l under different levels of applied strains ε_{22}. (**C**) Effect of δ/l on the stiffness in 33-direction (K_{33}) of the kirigami spikes with concave, triangle, and convex shapes with $\gamma = 30^{\circ}$ as a function of ε_{22}.
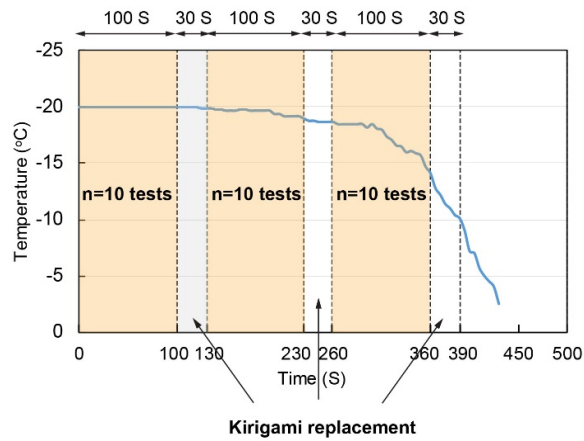
Fig. S13: Variation of ice surface temperature during human force plate measurement of friction with kirigami shoe grips. The temperature of ice blocks during the experiments was monitored using a K-type thermocouple embedded into the top surface. The average of temperature variations recorded over t=7 min for n=30 force-plate human tests (10 measurements per 100 S time periods with 30 S time interval between for replacing the kirigami shoe grips).

			P values
Fig. 3C **Concave**	Ice	μ_s (kirigami vs. control)	0.000912
		μ_k (kirigami vs. control)	0.000144
	Vinyl	μ_s (kirigami vs. control)	0.002367
		μ_k (kirigami vs. control)	0.032417
	Hardwood	μ_s (kirigami vs. control)	0.103851
		μ_k (kirigami vs. control)	0.000494
Fig. 3C **Triangle**	Ice	μ_s (kirigami vs. control)	0.023017
		μ_k (kirigami vs. control)	0.022258
	Vinyl	μ_s (kirigami vs. control)	0.093200
		μ_k (kirigami vs. control)	0.672700
	Hardwood	μ_s (kirigami vs. control)	0.031022
		μ_k (kirigami vs. control)	0.066804
Fig. 3C **Convex**	Ice	μ_s (kirigami vs. control)	0.015963
		μ_k (kirigami vs. control)	0.081590
	Vinyl	μ_s (kirigami vs. control)	0.002472
		μ_k (kirigami vs. control)	0.099844
	Hardwood	μ_s (kirigami vs. control)	0.026974
		μ_k (kirigami vs. control)	0.023503
Fig. 3F	Arrangement 1	μ_s (kirigami vs. control)	0.000912
		μ_k (kirigami vs. control)	0.000144
	Arrangement 2	μ_s (kirigami vs. control)	0.006200
		μ_k (kirigami vs. control)	0.001205
	Arrangement 3	μ_s (kirigami vs. control)	0.000134
		μ_k (kirigami vs. control)	0.000045
	Arrangement 4	μ_s (kirigami vs. control)	0.016297
		μ_k (kirigami vs. control)	0.022709
	Arrangement 5	μ_s (kirigami vs. control)	0.027102
		μ_k (kirigami vs. control)	0.010209

Table S1: Precise *P* values reported from the two-sample *t* tests used to determine the significance in Fig. 3.

Movie S1. Steel kirigami shoe grips attached to a shoe sole. The slip-resistant assistive kirigami metasurface attached to a shoe sole undergoes a shape transformation from a flat surface (corresponding to low friction) to the 3D textured surface with popped-up spikes (corresponding to high friction). This reversible shape transformation caused by bending of the show sole, which induces stretching in the patches, resulting in buckling out the spikes that enables us to tune friction actively and subsequent resistance to slips and falls.

Movie S2. Finite element simulation of kirigami unit cell. A periodic kirigami unit cell with concave spikes is initially stretched up to $\varepsilon_{22} = 0.15$ and then compressed in the normal direction by pushing down a rigid plate against it. The contours in top left panel shows distribution of max principal plastic strain during the deformation. The plastic strains localized in the hinges are moderate and the residual plastic strain is ~ 2%.